AGU PUBLICATIONS

Geophysical Research Letters

RESEARCH LETTER
10.1002/2015GL063558

Key Points:
- We study the spatiotemporal structure of seismic power in Long Beach (CA)
- Spatiotemporal filtering enhances signatures of moving traffic sources
- Velocity, acceleration, and counts of various events are measurable

Supporting Information:
- Text S1 and Figure S1

Correspondence to:
N. Riahi,
nriahi@ucsd.edu

Citation:
Riahi, N., and P. Gerstoft (2015), The seismic traffic footprint: Tracking trains, aircraft, and cars seismically, *Geophys. Res. Lett.*, *42*, doi:10.1002/2015GL063558.

Received 18 FEB 2015
Accepted 19 MAR 2015
Accepted article online 25 MAR 2015

The seismic traffic footprint: Tracking trains, aircraft, and cars seismically

Nima Riahi[1] and Peter Gerstoft[1]

[1] Scripps Institution of Oceanography, University of California, San Diego, La Jolla, California, USA

Abstract Although naturally occurring vibrations have proven useful to probe the subsurface, the vibrations caused by traffic have not been explored much. Such data, however, are less sensitive to weather and low visibility compared to some common out-of-road traffic sensing systems. We study traffic-generated seismic noise measured by an array of 5200 geophones that covered a 7 × 10 km area in Long Beach (California, USA) with a receiver spacing of 100 m. This allows us to look into urban vibrations below the resolution of a typical city block. The spatiotemporal structure of the anthropogenic seismic noise intensity reveals the Blue Line Metro train activity, departing and landing aircraft in Long Beach Airport and their acceleration, and gives clues about traffic movement along the I-405 highway at night. As low-cost, stand-alone seismic sensors are becoming more common, these findings indicate that seismic data may be useful for traffic monitoring.

1. Introduction

The ambient seismic wavefield has received much interest in the recent past both for its natural sources [*Gerstoft et al.*, 2006a; *Koper and de Foy*, 2008; *Kedar*, 2011; *Hillers et al.*, 2012] but also as a new probing signal for the solid Earth [*Sabra et al.*, 2005; *Gerstoft et al.*, 2006b; *Moschetti et al.*, 2007; *Riahi et al.*, 2013; *Weemstra et al.*, 2013] and to predict earthquake ground motion [*Denolle et al.*, 2014]. In comparison, anthropogenic seismic noise has received little attention so far [e.g., *Groos and Ritter*, 2009] or was only used indirectly for site amplification studies [*Bonnefoy-Claudet et al.*, 2006; *D'Amico et al.*, 2008] or subsurface imaging [*Nakata et al.*, 2011]. Seismic traffic noise, in particular, is an interesting observable: in contrast to traffic sensing systems based on video, infrared, acoustics, or radar, the vibrations caused by traffic are less affected by bad weather and limited visibility [*Wang et al.*, 2014].

In this work we study traffic-generated seismic energy in a geophone array that was deployed in the city of Long Beach (California, USA) as part of an industrial seismic survey. The array consisted of 5200 sensors that were spaced about 100 m apart and recorded with a sampling frequency of 250 Hz. Figure 1 shows the array configuration and a snapshot of seismic power across the network as measured on Monday, 7 March at 17:36 h. Originally designed for industrial active source imaging, the data have also been studied for passive source seismological purposes [*Lin et al.*, 2013; *Schmandt and Clayton*, 2013].

A large part of anthropogenic noise is typically of high frequency (>5 Hz) and may often be scattered and attenuated at relatively small distances. Previous work on seismic vehicle noise was thus based on denser sensor networks compared to the Long Beach array [*Stafsudd et al.*, 2007; *Wang et al.*, 2014]. However, the design does allow to study the time evolution of seismic power with a spatial resolution smaller than typical city blocks and road sections. At high frequencies this seismic power can be used as an indicator for seismic source proximity since seismic energy created by a surface source in Long Beach only dominates the wave field up to a distance comparable to the receiver spacing.

Moving seismic sources along given paths are then revealed through the use of a spatiotemporal analysis of seismic power. This allows us to study the Long Beach metro train movements, see departing and landing aircraft in the Long Beach airport, and even track certain slow moving vehicles along the I-405 highway.

2. Data Set and Processing

The seismic data were acquired by a geophone array that was deployed over an area of about 7 × 10 km in Long Beach (California, USA) as part of an industrial seismic survey (see Figure 1). The array consisted of 5200 geophones (OYO CT32D vertical velocity sensors with 10 Hz corner frequency) that were spaced about

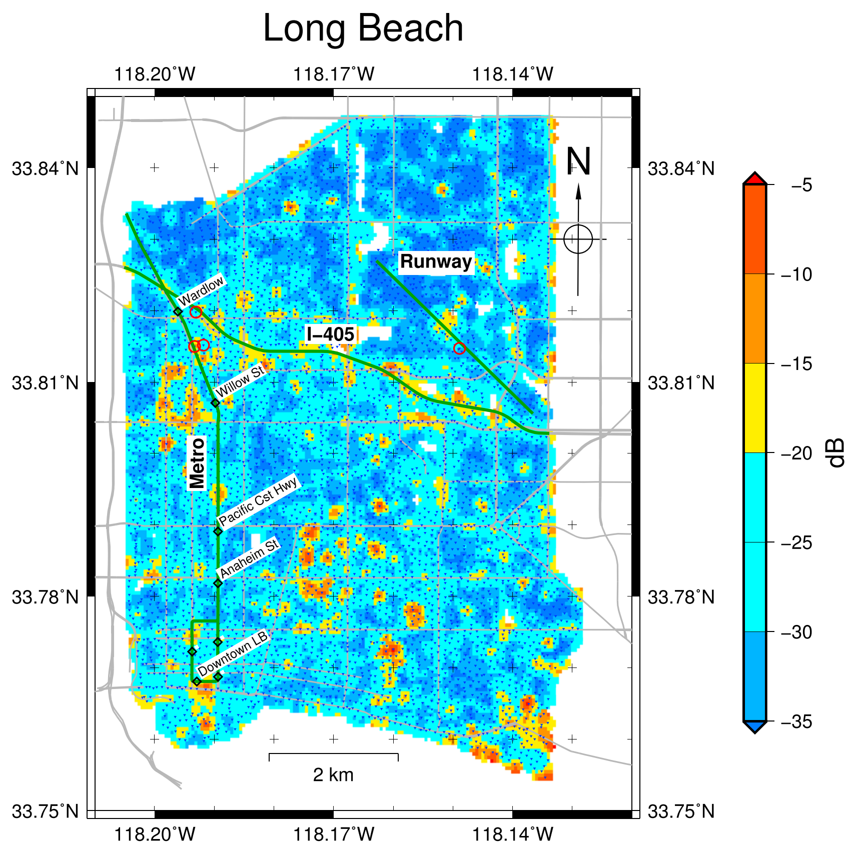

Figure 1. Snapshot of seismic noise power on Monday, 7 March at 17:36 h local time (averaged over 1 s), dB scale relative to $(m/s)^2$/Hz. The green paths indicate the Blue Line Metro track (black diamonds are metro stations), the I-405 highway, and a Long Beach Airport runway. Geophone locations (green triangles) and the grid of major roads (gray paths) are indicated.

100 m apart and recorded with a sampling frequency of 250 Hz. We analyze 1 week of the data in 2011 from 5 March at 16 h to 12 March at 8 h (161 h, time indications always refer to local time).

We use a section of the Metro Blue Line (roughly between Wardlow Station and Pacific Coast Highway Station) to illustrate our processing workflow. In the first step all receivers within 105 m of the metro track are selected. The velocity recordings $u(t)$ are converted to time series of seismic power, $P(t)$:

$$P(t) = \frac{1}{2K+1} \sum_{k=-K}^{K} u^2(t + k \cdot \Delta t_s) \,, \tag{1}$$

where Δt_s is the sampling period and $T = (2K+1)\Delta t_s = 1$ s is the window size and also chosen as the sampling period for the power (Figure 2a). The full frequency content of the geophone recordings is therefore considered (5–125 Hz). Second, we normalize $P(t)$ to have a standard deviation of one, $P_a(t) = P(t) - \mu/\sigma$, where μ and σ are sampling mean and standard deviation of $P(t)$ over the analysis period (typically less than 1 h). This step equalizes the time series variations among the traces and thus mitigates the effect of extremely noisy locations. Third, we compute a moving average with window length $T_{\mathrm{MA}} = (2L-1)T = 30$ s and subtract it from $P_a(t)$:

$$P_b(t) = P_a(t) - \frac{1}{2L-1} \sum_{l=-L}^{L} P_a(t + l \cdot T) \,. \tag{2}$$

This enhances variations in seismic power at time scales below T_{MA} such as passing vehicles while also reducing weakly varying portions such as continuously running machinery (see Figure 2b). In the fourth step the time series are spatially interpolated to a location $\mathbf{x}$ along the track using a distance-inverse weighting:

$$P_b(\mathbf{x}, t) = \sum_{|\mathbf{x}-\mathbf{x}_i|<r} w_i \cdot P_b(\mathbf{x}_i, t) \,, \tag{3}$$

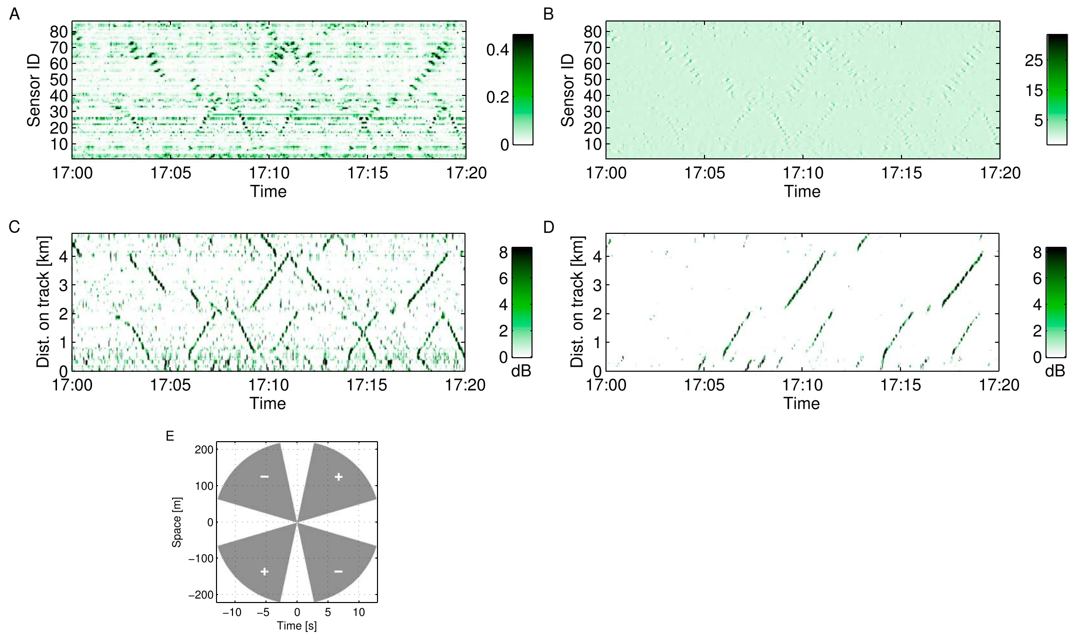

Figure 2. The processing steps are illustrated on data from a 4.5 km section of the metro track for Monday, 7 March between 17:00 h and 17:20 h (local time), increasing distance indicates southward movement. (a) Seismic power computed at all sensors with sampling period 1 s. Sensor ID is only loosely related to location along track. (b) After tracewise normalization and subtracting a moving 30 s average from the traces. (c) Traces are interpolated to the metro track, scaled to dB and lowest 70% are cropped. The sensor IDs are now mapped to physical distance along track. (d) Spatiotemporal filter reduces speckle noise and enhances motion along positive spatial direction. (e) A stencil defining four space-time areas around (0 m, 0 s). Positive areas capture trajectories for velocities between 5 and 80 m/s, negative areas relate to corresponding negative velocities. Color scales always map from the minimum to the maximum of the data.

where $\mathbf{x}_i$ is the location of sensor i, $r = 105$ m, and the weights are $w_i = \alpha/|\mathbf{x} - \mathbf{x}_i|$ with α such that the weights sum to one (for $\mathbf{x} = \mathbf{x}_k$ we set $w_i = \delta_{ik}$). Figure 2c shows P_b in dB scale with the lowest 70% of values cropped (minimum is set to 0 dB) which reduces weak interferers.

The fifth processing step is a spatiotemporal filter that emphasizes signals that persistently move in positive spatial direction over several seconds. These signals are local and often intermittent in the spatiotemporal domain, and we therefore chose a local filter that operates directly in that domain. We define a stencil $m(x, t)$ in a small spatiotemporal neighborhood Ω around $(x = 0, t = 0)$. The area covering all trajectories moving with positive velocity between 5 and 80 m/s through the center is given an equal positive weight in $m(x, t)$. Similarly, the area of negative velocities is weighted negatively (Figure 2e). For a point (x_0, t_0), let $D(x_0, t_0)$ be the difference between the average power in the positive and negative areas defined by centering m around (x_0, t_0):

$$D(x_0, t_0) = \sum_{(x,t)\in\Omega} m(x, t) \cdot P_b(x + x_0, t + t_0)\,, \tag{4}$$

where the positive and negative areas in $m(x, t)$ are scaled such that $\Sigma_{(x,t)\in\Omega} m(x, t) = 0$. We define a filter that sets $P_b(x_0, t_0)$ to zero if $D(x_0, t_0) < \xi$, where ξ is a filter design parameter and in this case was set to 1 dB based on empirical tests. Note that D can be computed effectively using digital image filtering techniques [e.g., *O'Gorman et al.*, 2008, p. 61], interpreting P_b as an image and m as a filter mask. After filtering the speckle and stationary sources are mostly reduced and motion in negative spatial direction (northward in this case) is removed (Figure 2d).

The spectral content and signal decay from moving sources is studied to validate using the full-frequency band (0–125 Hz) and interpreting seismic power as a source proximity indicator. We analyze two receivers slightly South of Wardlow Station at distances 15 and 155 m from the metro track (red circles in Figure 1).

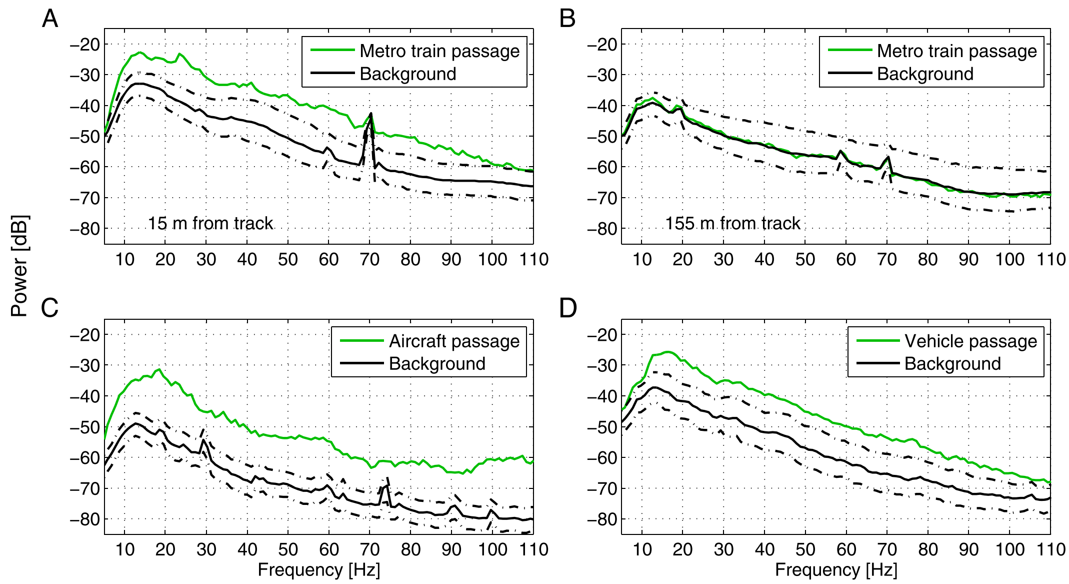

Figure 3. Median PSDs at four locations (red circles in Figure 1). (a) 7 March between 17 and 18 h, in a quiet area at the northern end of the metro track, 15 m and (b) 155 m from the track. Dash-dotted lines give the 25th–75th percentile range of background noise. (c) 6 March between 21 and 22 h close to the center of the airport runway. (d) 8 March between 01:45 and 02:15 h at a location less than 30 m from the I-405 highway.

Power spectral density (PSD) are estimated in 1 s time segments on 7 March between 17 and 18 h for segments with and without a train passing event. For the receiver next to the track, Figure 3a shows the median PSD of the background noise (black, no trains) and segments where a train passes (green, 22 train passages in total). The aggregate metro train spectrum is 5–10 dB higher than the background over 5–100 Hz. At 155 m from the track (Figure 3b) the metro passages have only a small effect (<1 dB) in the 10–20 Hz band. Thus, only receivers within 150 m from the track are used and no bandpass filtering is applied. At 20 Hz and assuming a weathered layer velocity of 400 m/s this corresponds to about $150\ \mathrm{m}/(\frac{400\ \mathrm{m/s}}{20\ \mathrm{Hz}}) \simeq 8$ wavelengths.

3. Metro Schedule

We apply the above workflow to the full length of the metro track within the array for a 1 h analysis period starting on 7 March at 17:00 h. Seismic power time series are computed and interpolated to the track (equation (4)) and cropped at 8 dB below the maximum. The result is a summary of vibrational activity along the train track with the spatiotemporal structure of the metro already visible (Figure 4a): it enters from the north, moves southward, loops in downtown Long Beach, and returns northward (the spatial coordinate increases accordingly). The raw seismic power is, however, strongly affected by stationary and transient noise generated by nonmoving infrastructure or moving sources not aligned with the track. There are particularly large levels of interference in the downtown Long Beach loop between 6.5 and 9 km (see also Figure 1). Outside the loop the moving sources have two directions due to the topology of the metro track.

The processing substantially removes speckles (in space-time) and continuous, nonmoving noise sources (e.g., near Wardlow Station), as seen in Figure 4b. Metro train movement is visible even between Willow Street and Anaheim where the metro moves along Long Beach Boulevard, a main traffic road. Analysis of northbound trains moving along this road (south of Willow Street Station) gives velocities of 16–18 m/s (35–40 mph) while velocities in the following section to the north (isolated tracks) increase to 20–25 m/s (44–55 mph). The source movement is interrupted for a few minutes around the metro stations, but also on some other locations which coincide with traffic crossings. During rush hour the train frequency from Los Angeles to Willow Street Station (<3.2 km and >12.6 km) is twice that of the section farther south. The red circle in Figure 4b can be matched with a power anomaly north of Pacific Coast Highway Station in Figure 1. The limits of the workflow are reached in downtown Long Beach where no signal is recovered.

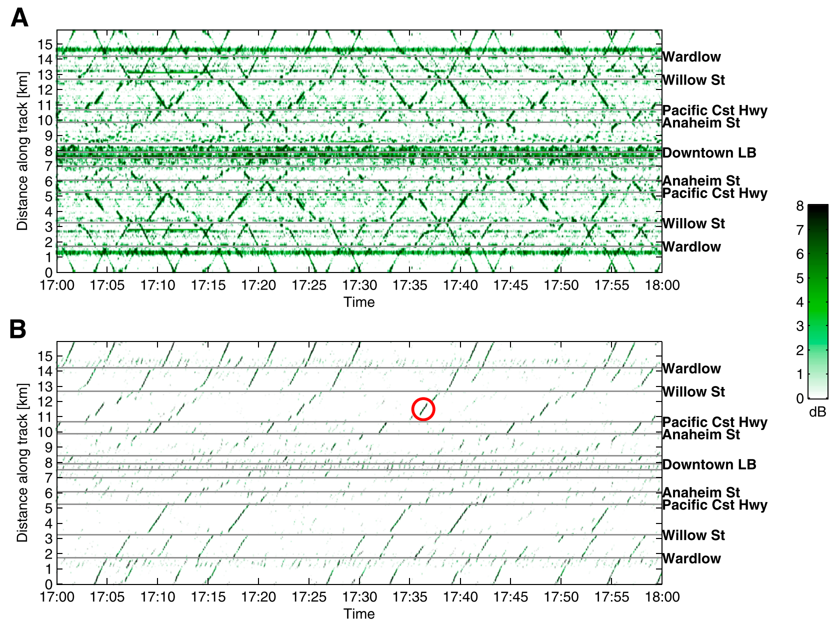

Figure 4. Seismic power measured along the metro track during rush hour on 7 March from 17 to 18 h. (a) Raw seismic power is compared to (b) the spatiotemporally filtered version. The metro enters the array from the north (0 km), proceeds to the downtown Long Beach loop at 6.6 km, and leaves the loop again at 9.3 km to travel back northward. Black lines indicate metro stations along the track. The red circle in Figure 4b indicates a section that is visible as slightly elevated levels on the power snapshot map in Figure 1(north of Pacific Coast Highway Station).

4. Long Beach Airport Runway

Next we describe how aircraft motion can be extracted from runway sensors, allowing to estimate some runway velocities. The analysis includes 74 receivers within a 105 m distance of the main southwest-to-northeast runway at Long Beach Airport. Seismic power is computed from 21 to 22 h on Sunday, 6 March, and shown in Figure 5a. Stationary and continuous noise is a common occurrence in the airport seismic power measurements, but some weak subvertical streaks are visible that hint at aircraft motion.

To account for the faster velocities expected on an airport runway, the power sampling period is reduced to 0.5 s and the spatiotemporal filtering is adapted for velocities between 10 and 200 m/s and a higher threshold value of 3 dB is used due to the increased signal-to-interference ratio near the runway. The processed seismic power is shown in Figure 5b: four large and five smaller streaks are clearly visible. The PSD of these passing aircraft are compared with background noise in Figure 3c for a receiver half-way down the runway (red circle in Figure 1). A strong power increase between 10 and 20 dB is observed over 5–110 Hz, confirming that the full-frequency band can be used.

Two portions of the data in Figure 5b are shown in Figures 5c and 5d: the more and less elongated features show an accelerating and decelerating pattern, respectively, identifying these events as departing and landing aircraft. We compute a least squares fit of a constant acceleration model ($x = \frac{1}{2}at^2 + v_0t + x_0$) to these events. For the departing aircraft we estimate an acceleration of 1.0 m/s^2 and takeoff velocity of 80 m/s (about 288 km/h). The landing aircraft has an estimated acceleration of −1.8 m/s^2 and touchdown velocity of 69 m/s (about 248 km/h). Note that the above measurements are based on a subjective assessment about when a substantial amount of seismic energy emerges (red circles in Figures 5c and 5d) and should be interpreted with caution. The range of effective takeoff and touchdown velocities depends on many factors such temperature, wind, aircraft type, aircraft weight, and flap position. While these factors are unknown, the observed velocities are reasonable and could correspond to, e.g., an Embraer 175 under normal circumstances.

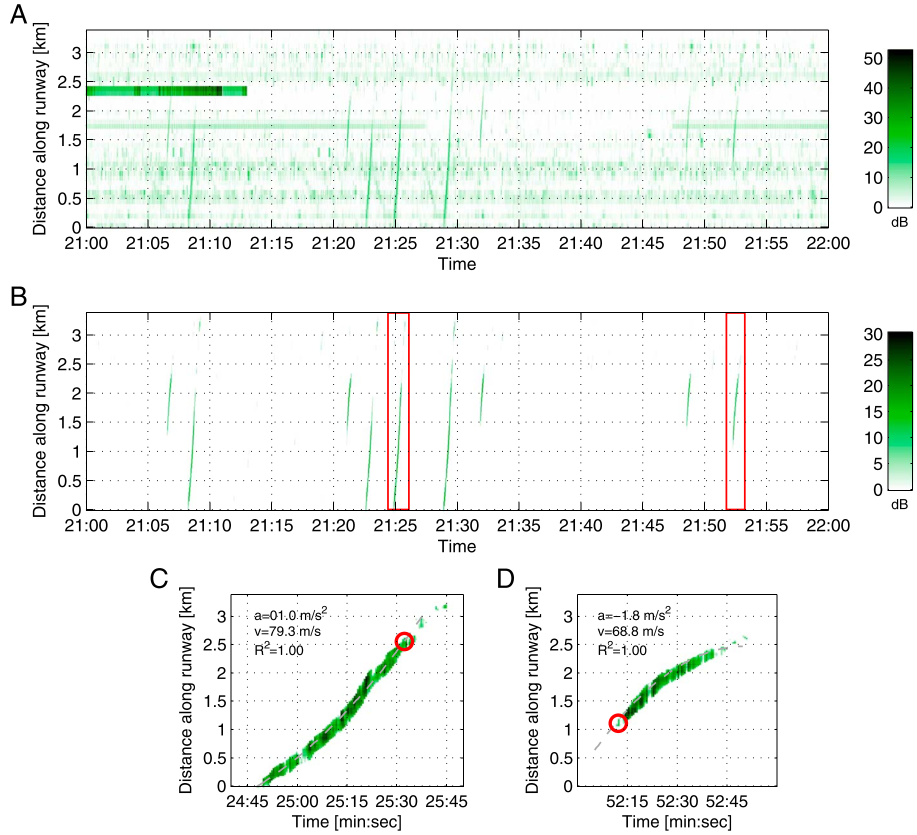

Figure 5. (a) Raw seismic power measured along the runway from southeast (0 km) to northwest (3.3 km). (b) Processed seismic power. (c) Zoom-in on an aircraft taking off toward northwest (accelerating at 1.3 m s^{-2}, left red box in Figure 5b) and (d) landing from southeast (acceleration of −1.5 m s^{-2}, right red box in Figure 5b). Dashed line in Figures 5c and 5d is a fitted acceleration parabola.

During the 161 h that were analyzed there were a total of 297 departures and 314 arrivals with signatures similar to the ones shown in Figures 5c and 5d. The runway statistics for the analyzed period are no longer available, but the airport is used by many small aircraft which may not have been detected by this analysis.

5. Traffic

Using data from a single acoustic recording it has been shown that overall traffic density at a point in a highway can be accurately estimated [*Tyagi et al.*, 2012]. We apply our workflow on the 7.3 km section of the I-405 highway that crosses the Long Beach array to assess how well individual vehicles may be identified using our workflow. For the most part that highway section carries two-way traffic on 10 lanes and traffic density and velocity should vary strongly over the day. There are 97 receivers within 105 m to the lateral center of the highway, leaving about 13 sensors for every kilometer of highway. Seismic power is interpolated to the center of the highway, and the separation of eastward and westward moving sources is attained using the spatiotemporal filter.

Figure 6a gives filtered seismic power computed for eastward traveling sources on the highway at night (0 km is to the east). The same parameters are used as for the Metro case, except the dynamic range is constrained to 30th–80th percentiles. There are isolated, regularly moving sources that cross the entire highway section uninterrupted. A histogram of measured velocities from 25 such events is shown in Figure 6b. The observed average velocity is 26 m/s (58 mph) with standard deviation 2 m/s (4 mph) which is close to the speed limit of 55 mph for trucks and some special vehicles, implicating such vehicles as vibrationally dominant sources on the highway. The PSD of these passing vehicles is compared with background noise in Figure 3d for a receiver 30 m from the highway shoulder. As with the metro and airport examples, a broadband power increase is observed.

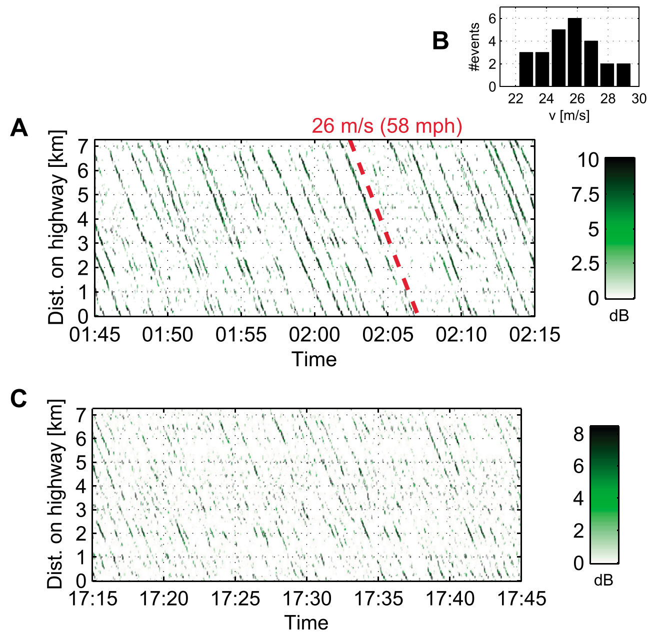

Figure 6. Processed seismic power along the I-405 highway filtered for eastward moving sources on (a) Tuesday night between 01:45 and 02:15 h, and (c) Monday afternoon between 17:15 and 17:45 h. (b) Histogram of velocities of sources in Figure 6a. The average velocity is 26 m/s (58 mph).

Filtered seismic power during Monday rush hour is mostly cluttered (Figure 6c). Intriguingly, there are still some isolated sources visible that move uninterrupted for about 0.5–2 km through the highway. The velocity for eight such sources is measured and yields an average of 25 $\pm$ 3 m/s (57 $\pm$ 6 mph). These sources may be due to trucks or vehicles moving along special lanes reserved for high-occupancy vehicles on the studied section of the highway. The true cause cannot be verified because no traffic data are available for this time period.

6. Conclusions

We have studied traffic-related seismic vibrations measured by an urban geophone network with a spacing slightly shorter than a typical city block dimension. The spatiotemporal structure of vibrational intensity allows us to measure a metro train schedule, compute runway statistics and aircraft motion parameters, and even track larger vehicles on a highway at night.

Seismic power is used here as an indicator for source proximity because in most cases this attribute is sufficient and robust when the source is within a receiver spacing from the source. Although this limits resolution to about half the sensor spacing, it does enable the tracking of strong moving sources over several receiver spacings even in the presence of many interferers. This could be further exploited for real-time traffic monitoring since seismic power is easily computed and transmitting it requires low bandwidth (about one measurement per second). As seismic data are becoming more common, they may therefore be a useful source for large-scale traffic monitoring, in particular since they are less sensitive to weather and low visibility.

Acknowledgments
We thank NodalSeismic LLC and Signal Hill Petroleum Inc. for sharing the data, in particular Dan Hollis and Robert Clayton for their efforts in making the data available. We also thank our two anonymous reviewers for helping to improve the manuscript. This work is supported by NSF grant EAR-0944109 and by the Swiss National Science Foundation.

The Editor thanks two anonymous reviewers for their assistance in evaluating this paper.

References

Bonnefoy-Claudet, S., F. Cotton, and P.-Y. Bard (2006), The nature of noise wavefield and its applications for site effects studies: A literature review, *Earth Sci. Rev.*, *79*, 205–227.

D'Amico, V., M. Picozzi, F. Baliva, and D. Albarello (2008), Ambient noise measurements for preliminary site-effects characterization in the urban area of Florence, Italy, *Bull. Seismol. Soc. Am.*, *98*(3), 1373–1388, doi:10.1785/0120070231.

Denolle, M. A., E. M. Dunham, G. A. Prieto, and G. C. Beroza (2014), Strong ground motion prediction using virtual earthquakes, *Science*, *343*(6169), 399–403, doi:10.1126/science.1245678.

Gerstoft, P., M. C. Fehler, and K. G. Sabra (2006a), When Katrina hit California, *Geophys. Res. Lett.*, *33*, L17308, doi:10.1029/2006GL027270.

Gerstoft, P., K. G. Sabra, P. Roux, W. A. Kuperman, and M. C. Fehler (2006b), Green's functions extraction and surface-wave tomography from microseisms in southern California, *Geophysics*, *71*(4), SI23–SI31, doi:10.1190/1.2210607.

Groos, J. C., and J. R. R. Ritter (2009), Time domain classification and quantification of seismic noise in an urban environment, *Geophys. J. Int.*, *179*(2), 1213–1231, doi:10.1111/j.1365-246X.2009.04343.x.

Hillers, G., N. Graham, M. Campillo, S. Kedar, M. Landes, and N. Shapiro (2012), Global oceanic microseism sources as seen by seismic arrays and predicted by wave action models, *Geochem. Geophys. Geosyst.*, *13*, Q01021, doi:10.1029/2011GC003875.

Kedar, S. (2011), Source distribution of ocean microseisms and implications for time-dependent noise tomography, *C.R. Geosci.*, *343*(8–9), 548–557, doi:10.1016/j.crte.2011.04.005.

Koper, K. D., and B. de Foy (2008), Seasonal anisotropy in short-period seismic noise recorded in south Asia, *Bull. Seismol. Soc. Am.*, *98*(6), 3033–3045, doi:10.1785/0120080082.

Lin, F., D. Li, R. Clayton, and D. Hollis (2013), High-resolution 3D shallow crustal structure in Long Beach, California: Application of ambient noise tomography on a dense seismic array, *Geophysics*, *78*(4), Q45–Q56, doi:10.1190/geo2012-0453.1.

Moschetti, M. P., M. H. Ritzwoller, and N. M. Shapiro (2007), Surface wave tomography of the western United States from ambient seismic noise: Rayleigh wave group velocity maps, *Geochem. Geophys. Geosyst.*, *8*, Q08010, doi:10.1029/2007GC001655.

Nakata, N., R. Snieder, T. Tsuji, K. Larner, and T. Matsuoka (2011), Shear wave imaging from traffic noise using seismic interferometry by cross-coherence, *Geophysics*, *76*(6), SA97–SA106, doi:10.1190/geo2010-0188.1.

O'Gorman, L., M. Sammon, and M. Seul (2008), *Practical Algorithms for Image Analysis: Description, Examples, and Code*, vol. 1, Cambridge Univ. Press, New York.

Riahi, N., G. Bokelmann, P. Sala, and E. H. Saenger (2013), Time-lapse analysis of ambient surface wave anisotropy: A three-component array study above an underground gas storage, *J. Geophys. Res. Solid Earth*, *118*, 5339–5351, doi:10.1002/jgrb.50375.

Sabra, K. G., P. Gerstoft, P. Roux, W. A. Kuperman, and M. C. Fehler (2005), Surface wave tomography from microseisms in southern California, *Geophys. Res. Lett.*, *32*, L14311, doi:10.1029/2005GL023155.

Schmandt, B., and R. W. Clayton (2013), Analysis of teleseismic P waves with a 5200-station array in Long Beach, California: Evidence for an abrupt boundary to Inner Borderland rifting, *J. Geophys. Res. Solid Earth*, *118*, 5320–5338, doi:10.1002/jgrb.50370.

Stafsudd, J. Z., R. E. Hudson, E. Taciroglu, and K. Yao (2007), Seismic-array signal processing for moving source localization, in *Proceedings SPIE 6697, Advanced Signal Processing Algorithms, Architectures, and Implementations XVII, San Diego, Calif., 26–27 Aug. 2007*, edited by F. T. Luk, pp. 66970H–1–66970H-12, SPIE, Bellingham, Washington, D. C., doi:10.1117/12.732713

Tyagi, V., S. Kalyanaraman, and R. Krishnapuram (2012), Vehicular traffic density state estimation based on cumulative road acoustics, *IEEE Trans. Intell. Transp. Syst.*, *13*(3), 1156–1166, doi:10.1109/TITS.2012.2190509.

Wang, H., W. Quan, Y. Wang, and G. R. Miller (2014), Dual roadside seismic sensor for moving road vehicle detection and characterization, *Sensors*, *14*(2), 2892–910, doi:10.3390/s140202892.

Weemstra, C., L. Boschi, A. Goertz, and B. Artman (2013), Seismic attenuation from recordings of ambient noise, *Geophysics*, *78*(1), Q1–Q14, doi:10.1190/geo2012-0132.1.

